



Visualizing the growth process of sodium microstructures in sodium batteries by in-situ ^{23}Na MRI and NMR spectroscopy

Yuxuan Xiang¹, Guorui Zheng¹, Ziteng Liang¹, Yanting Jin², Xiangsi Liu¹, Shijian Chen¹, Ke Zhou¹, Jianping Zhu¹, Min Lin¹, Huajin He¹, Jiajia Wan¹, Shenshui Yu¹, Guiming Zhong³✉, Riqiang Fu⁴, Yangxing Li⁵ and Yong Yang¹✉

The growth of sodium dendrites and the associated solid electrolyte interface (SEI) layer is a critical and fundamental issue influencing the safety and cycling lifespan of sodium batteries. In this work, we use in-situ ^{23}Na magnetic resonance imaging (MRI) and nuclear magnetic resonance (NMR) techniques, along with an innovative analytical approach, to provide space-resolved and quantitative insights into the formation and evolution of sodium metal microstructures (SMSs; that is, dendritic and mossy Na metal) during the deposition and stripping processes. Our results reveal that the growing SMSs give rise to a linear increase in the overpotential until a transition voltage of 0.15 V is reached, at which point violent electrochemical decomposition of the electrolyte is triggered, leading to the formation of mossy-type SMSs and rapid battery failure. In addition, we determined the existence of NaH in the SEI on sodium metal with ex-situ NMR results. The poor electronic conductivity of NaH is beneficial for the growth of a stable SEI on sodium metal.

Sodium-based batteries have attracted a great deal of interest in recent years due to the abundance and low cost of sodium resources. A sodium metal anode provides a high theoretical specific capacity of $1,165 \text{ mA h g}^{-1}$ and a low voltage of -2.71 V versus the standard hydrogen electrode, which makes it an ideal anode material for sodium batteries. Nevertheless, the formation of sodium metal microstructures (SMSs), that is, dendritic and mossy-like Na metal, and the associated accumulation of a solid electrolyte interface (SEI) layer restrict its practical applications. Organic electrolytes are easily decomposed to form a thick and loosely packed SEI layer on the surface of Na metal during cycling. As a result, uneven Na nucleation and electrodeposition accelerate the growth of SMSs, which in return generate large amounts of new interfaces and the growth of a new SEI¹, which eventually leads to battery failure and even short circuiting.

To address these issues, diverse strategies have been developed, including modifying the interfacial layer^{2,3} and employing well-designed three-dimensional hosts and solid-state electrolytes⁴⁻⁶. However, the growth of SMSs is a transient process, and it is difficult to characterize SMSs by conventional post-mortem analytical methods. In-situ optical spectroscopy has been applied to provide direct observation of the evolution of Na deposition and gas evolution⁷, but the chemical components and space-resolved characterization could not be obtained. Although in-situ electron microscopy can provide chemical information and high-resolution images, the influence of the electron beam on the fragile Na dendrites should be addressed⁸.

Recently, nuclear magnetic resonance (NMR), a non-destructive and quantitative technique, has been applied to study the interface

between the anode and the electrolyte⁹⁻¹¹. NMR can distinguish the signals of metal microstructures on the surface from those in the bulk because the radiofrequency fields can only penetrate to a limited depth in the metal sample (the skin-depth effect)¹². For the Li metal anode, in-situ ^7Li NMR has proved to be a powerful method to monitor and quantify the growth of Li metal microstructures¹². Moreover, ^7Li magnetic resonance imaging (MRI) with space-resolved capability has been employed to monitor the morphologies of the deposited Li metal^{13,14}. Since Na metal is more reductive than Li metal, deposited Na metal has a thicker SEI layer and a rougher morphology¹⁵⁻¹⁷. Moreover, the deposition behaviour of Na metal is more complex than that of Li metal. The growth and evolution processes of sodium microstructures, along with their impact on electrochemical performance, are far less well understood. Although the correlation between growth of metal microstructures and the SEI for both Li and Na metals has been emphasized in previously reported work¹⁸⁻²⁰, a quantitative investigation of the composition and corresponding growth kinetics of the SEI layers is still lacking.

Here, we report the use of a combination of different characterization techniques, including in-situ MRI and operando NMR spectroscopy, together with high-resolution NMR, scanning electron microscopy (SEM), X-ray photoelectron spectroscopy (XPS) and electrochemical tests, to offer an in-depth understanding of the intrinsic correlations between the evolution of SMSs, the compositions of SEIs and their corresponding electrochemical features. Through in-situ ^{23}Na MRI, we provide information about both the spatial distribution and the morphological evolution process of SMSs. By employing an innovative analytical approach in

¹State Key Laboratory for Physical Chemistry of Solid Surfaces, Collaborative Innovation Center of Chemistry for Energy Materials and Department of Chemistry, College of Chemistry and Chemical Engineering, Xiamen University, Xiamen, China. ²Department of Chemistry, University of Cambridge, Cambridge, UK. ³Xiamen Institute of Rare Earth Materials, and Fujian Institute of Research on the Structure of Matter, Haixi Institutes, Chinese Academy of Sciences, Xiamen, China. ⁴National High Magnetic Field Laboratory, Tallahassee, FL, USA. ⁵4135 Belle Meade Circle, Belmont, NC, USA.

✉e-mail: gmgzhong@fjirsm.ac.cn; yyang@xmu.edu.cn

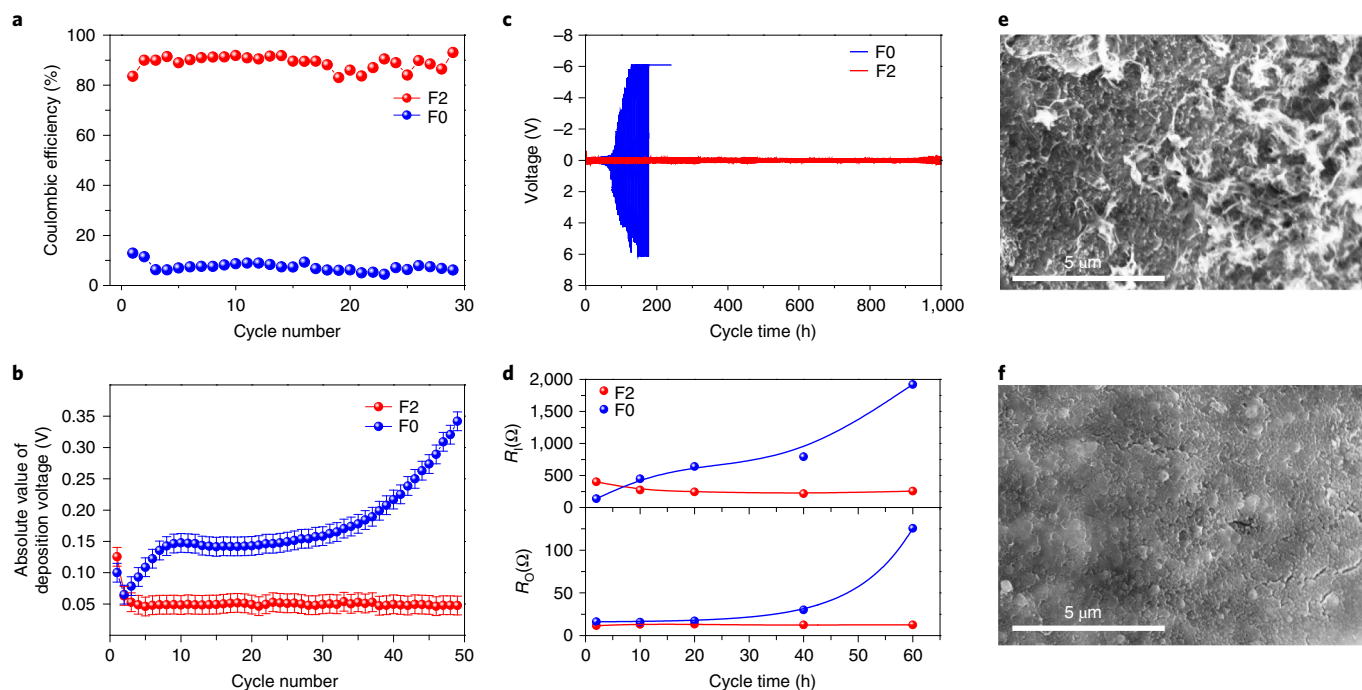


Fig. 1 | Electrochemical performances and morphologies of Na metals cycled with different electrolytes. a, Coulombic efficiencies of Na||Cu cells cycled with a capacity limit of 0.5 mA h cm^{-2} at 0.5 mA cm^{-2} using $1 \text{ M NaClO}_4/\text{PC}$ with 2% FEC (F2) and without FEC (F0) electrolytes. **b**, The corresponding absolute value of deposition voltages for Na deposit on the Cu foil. Error bars come from different cells for each electrolyte. **c**, Long-term cycling of Na||Na cells using F0 and F2 electrolytes, with a capacity limit of 1 mA h cm^{-2} at 0.5 mA cm^{-2} . **d**, The interfacial resistance (R_i) and ohmic resistance (R_o) for the Na||Na cells using F2 and F0 electrolytes. The data points are fitted by a single line to better show the trend of the increase. **e, f**, SEM images of Na metal after 50 cycles with 0.5 mA h cm^{-2} at 0.5 mA cm^{-2} without (**e**) and with (**f**) 2% FEC.

processing the operando ^{23}Na NMR data, we observe a clear correlation between the amounts of SMSs and the Na deposition overpotential. We also find NaH as an unexpected species in the SEI layers on Na metal.

Electrochemistry and deposition morphology

In the current study, two contrasting stripping and deposition behaviours are selected (Supplementary Fig. 1) by employing $1 \text{ M NaClO}_4/\text{propylene carbonate (PC)}$ with 2% fluoroethylene carbonate (FEC) (abbreviated as F2) and without FEC (F0) electrolytes. In Na||Cu cells, the cell with F0 electrolyte (the F0 cell) presents a very poor Coulombic efficiency (CE) below 10%, while the F2 cell yields a much higher CE of 88% in the first cycle, and its CE then stabilizes in the following cycles (Fig. 1a). The F2 cell shows a stable deposition voltage at around 0.05 V, indicating that a stable interface layer is formed (Fig. 1b). In contrast, the deposition voltage of the F0 sample increases from 0.05 V to 0.15 V during the first ten cycles, then stabilizes at around 0.15 V during the 10th to 30th cycles. Afterwards, an accelerated voltage increase to 0.35 V at the 50th cycle is observed. The results demonstrate that the failure mechanism of F0 may be divided into three stages, and the plateau at around 0.15 V is highly correlated to the consumption of electrolyte. The cell with more electrolyte shows a longer plateau (Supplementary Fig. 2).

Na||Na symmetric cells further indicate the contrast between F0 and F2 cells (Fig. 1c)³. The overpotential of the F0 cell increases dramatically during the initial cycles, and reaches 1 V only after 81 h of cycling. The F2 cell could cycle for more than 960 h with a constant overpotential, suggesting that a stable interface is generated with the addition of FEC, as evidenced by the electrochemical impedance measurements (EIS) and SEM results (Fig. 1d). For the F2 sample, the interfacial resistance (R_i) and the ohmic resistance (R_o) remain

almost constant during cycling. For the F0 sample, R_i increases gradually from 137.6 to 1,921.0 Ω , indicating a continuous accumulation of SEI and dead Na metal. R_o shows a notable increase after 10 cycles, verifying a large consumption of electrolytes in this stage. SEM images show a non-uniform and dendritic morphology when using F0 electrolyte (Fig. 1e). In sharp contrast, the F2 electrolyte leads to compact and uniform deposition of Na (Fig. 1f). As mentioned above, adding FEC provides a unique way to model, with uniform Na deposition and therefore good performance, offering a striking contrast to the F0 system.

In-situ ^{23}Na MRI study

How SMSs grow and evolve is closely related to battery failure. Here, we use the in-situ one-dimensional (1D) ^{23}Na MRI technique to characterize the cross-sections of SMSs in Na||Cu cells, and to detect Na distribution during cycling in a non-destructive way. Benefiting from the different chemical shifts of Na metal ($\sim 1,130 \text{ ppm}$) and the SEI components ($\sim 0 \text{ ppm}$), ^{23}Na MRI can be used to monitor the morphology of Na metal without interference from the SEI signal, thereby obtaining images of Na metal during cycling. Details of the in-situ MRI and operando NMR experiments are presented in Supplementary Fig. 3.

In this study, we adopt the Na||Cu cell configuration for MRI study, which allows us to directly observe the evolution of the electrochemistry-related sodium metal microstructures on the copper substrate, by avoiding interference from the bulk sodium metal signal. Figure 2 shows ^{23}Na MRI images of the Cu substrate in the first cycle of Na||Cu cells with F0 and F2 electrolytes. The images show the distribution of Na metal along the cross-section. After deposition, the Na metal signal was observed on the Cu foil for both electrolytes. The intensity of the Na metal signal for the cell with F2 electrolyte is lower than for F0. Since the cells were all limited to

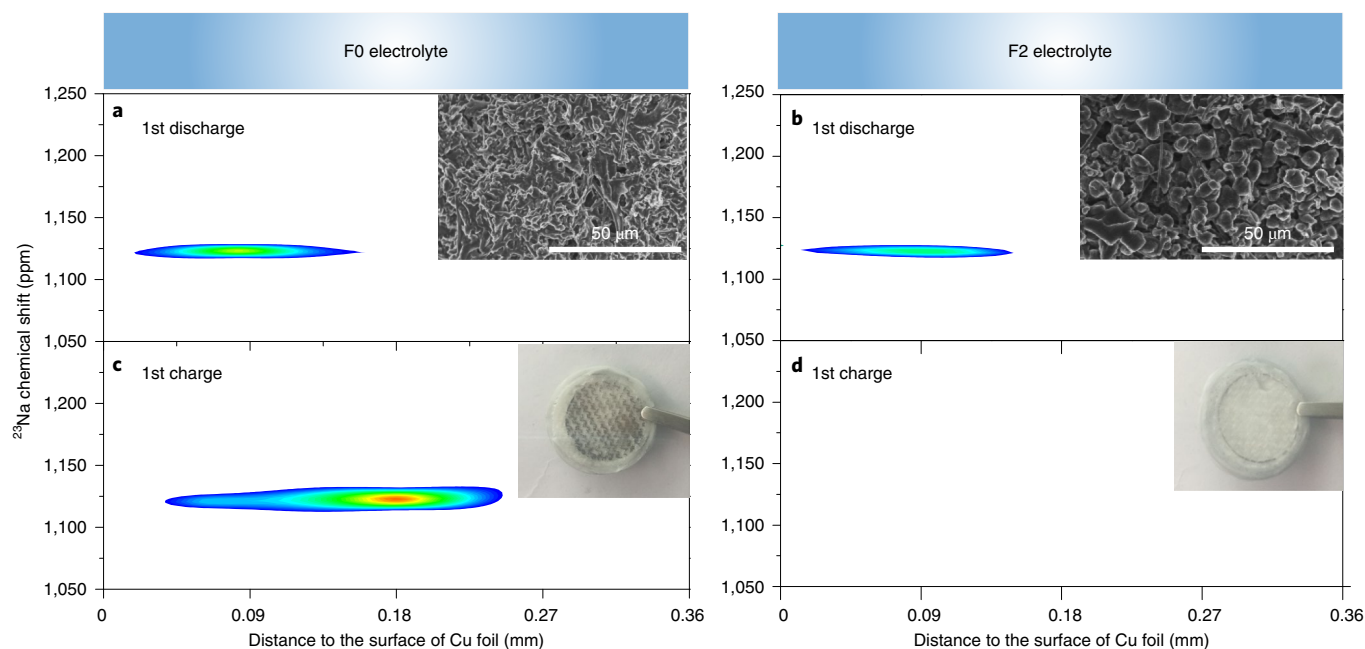


Fig. 2 | In-situ ^{23}Na metal MRI images of the Na||Cu batteries during the first cycle in F0 and F2 electrolytes. a–d, We referenced the distance against the Cu current collector as 0 mm. The insets of **a** and **b** show the SEM images of the deposited Na metal on the Cu foil after first discharge (that is, deposition). The insets of **c** and **d** are digital images of glass fibre after the first charge (that is, stripping).

the sample capacity, we would assume that the same amount of Na metal is deposited onto the Cu substrate. The lower intensity of the F2 sample is probably due to the issue of NMR skin depth and the results indicate that the F2 sample has a smaller specific surface area of deposited Na metal. The results are verified by SEM images. As shown in the insets of Fig. 2a,b, the Na metal deposited on the Cu foil with the F2 electrolyte yields larger sized particles, which leads to a smaller specific surface area. After stripping, MRI results show that the Na metal signal vanishes on the Cu foil with F2 electrolyte, indicating that the deposited Na metal is completely stripped (Fig. 2d). In the F0 sample, however, a strong signal from 0.09 mm to 0.18 mm is observed after stripping, indicating that most of the deposited Na metal is disconnected from the current collector and forms the dead Na metal (Fig. 2c). It worth noting that the digital optical image (Fig. 2c, inset) shows that the dead Na metal is mainly attached to the glass fibre, rather than remaining on the Cu foil. A similar result was also observed for the Li metal anode by operando optical spectroscopy²¹.

Figure 3a,b shows the ^{23}Na MRI images acquired at the end of the charge in the different cycles with F0 and F2 electrolytes, respectively. At the Na metal anode side (0.45 mm), the intensities of the Na metal signals for both electrolytes barely change as a function of cycling. For F0 electrolyte, the Coulombic efficiency of the cell is low, thus only a small amount of SMSs are formed on the Na metal and the intensity is difficult to be observed due to the strong Na metal signal. For the sample cycled in F2 electrolyte, smooth deposition is observed and so the formation of SMSs is much less. Of note is that the images were collected at the stripped states, thus the observed Na metal signals on the Cu foil are attributed to the dead SMSs. For F2, no Na metal signal is detected on the Cu foil after 15 cycles (Fig. 3b), indicating a highly reversible deposition/stripping process. For F0, on the other hand, the signal intensity of the dead Na metal increases and broadens over time, indicating a continuous expansion of SMSs (Fig. 3a). The MRI results also suggest that accumulation of the dead SMSs is continuous and cannot be reversed. The accumulation of SMSs would hinder the migration of Na^+ ions to the surface of Cu, and that increases the deposition

overpotential at a constant rate, as shown in Supplementary Fig. 5. Of note is that the space-resolved MRI images for the F0 electrolyte show that the dead SMSs first emerge at a position away from the Cu foil (at 0.18 mm) at the 1st charge state (Fig. 3a), and then grow bilaterally with cycling. They start to be parasitic on the Cu foil (at 0.09 mm) at the 5th charge state, and grow into the inside of the electrolyte (at 0.27 mm) at the 10th charge state. Consequently, a dead Na metal layer on the Cu foil ranging from 0 mm to 0.36 mm is formed at the 15th charge state. The thickness of the dead Na layer is further confirmed by SEM, as shown in Supplementary Fig. 9. To illustrate the process for F0 clearly, we divide the process into three stages. During the initial cycles (stage I), the morphologies of the deposited Na metal are more likely to be dendritic, the bottom part of which would dissolve upon stripping²², generating dead Na metal away from the Cu foil. After five cycles (stage II), severe decomposition of the electrolyte is likely to take place in this process (the deposition overpotential at this time is greater than 0.15 V, as shown in Supplementary Fig. 5). The electrolyte prefers to decompose at the tip of the Na metal, due to its higher local current density and larger ionic concentration gradient²³, which generates a large number of decomposition products that accumulate at the tip. These products would inhibit growth of the Na metal along the axial direction, producing more branches and leading to mossy-like SMSs that are parasitic on the Cu foil²⁴. In stage III, the formation of such new, mossy-like SMSs pushes the previously generated SMSs outward from the Cu foil. A porous dead Na metal layer eventually forms and blocks the transport pathway for Na^+ ions, causing a continuous increase in deposition overpotential (Supplementary Fig. 5). Therefore, we consider the overpotential as an important indicator of the operating condition of Na batteries.

Operando ^{23}Na NMR and quantitative insights

We now study the influence of the formation of SMSs on the subsequent electrochemical performance using an operando NMR experiment on the Na||Na symmetric cells, which allows us to gain quantitative information. The Na||Na symmetric cells used for NMR study present similar electrochemical performances to

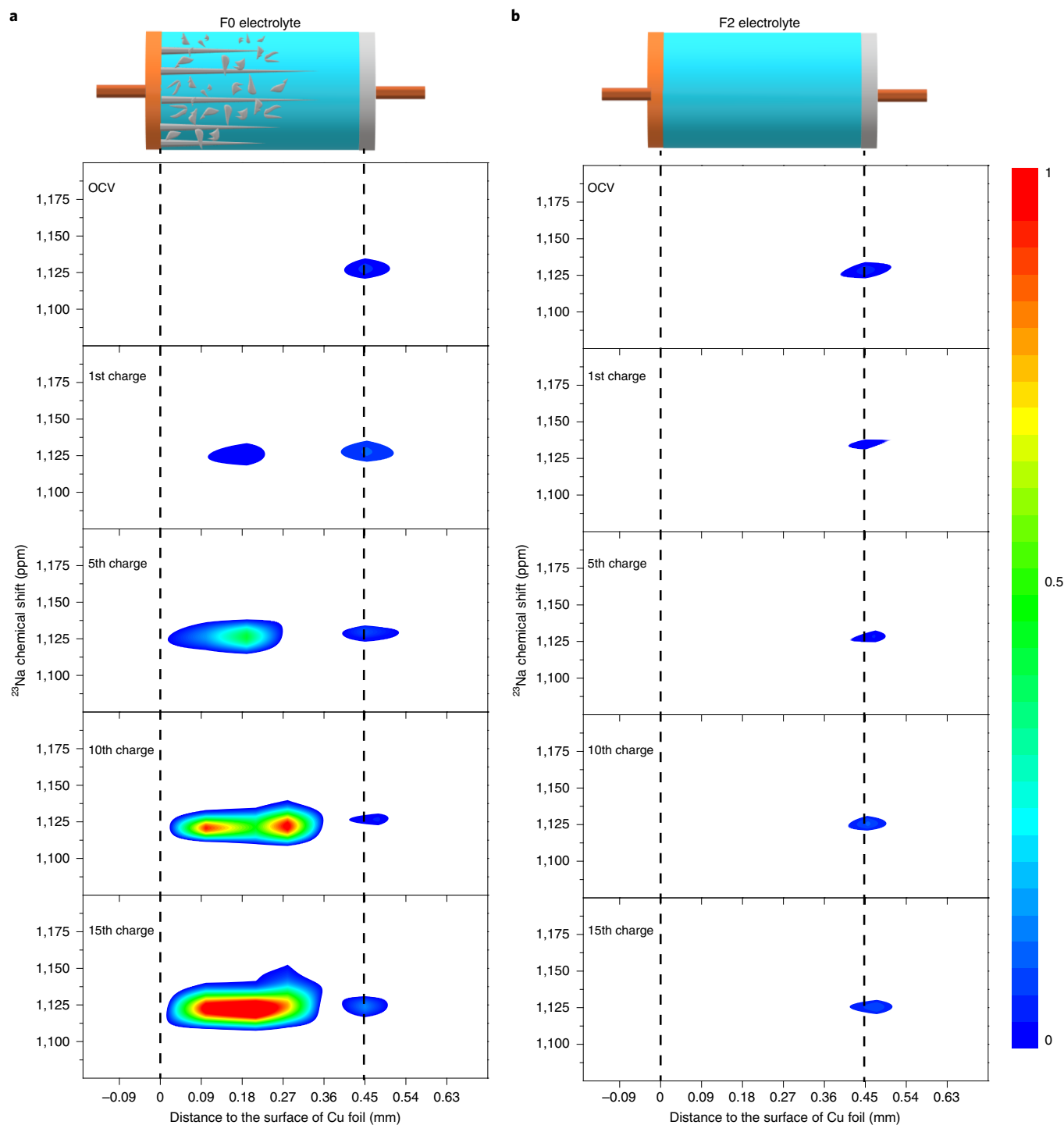


Fig. 3 | In-situ ^{23}Na metal MRI images of the Na||Cu batteries. a,b, The MRI experiments performed with F0 (**a**) and F2 (**b**) electrolytes at different charging states. The surface of the Cu foil is referenced as 0 mm and the Na metal anode is located 0.45 mm away from the Cu foil. The gap between Na and Cu is filled with glass fibre soaked with electrolyte. The contour plot shows the signal intensity of the Na metal with a chemical shift around 1,130 ppm. The representative one-dimensional ^{23}Na MRI spectra are shown in Supplementary Fig. 4.

Na||Na symmetric coin cells, as shown in Fig. 4a. It should be noted that the increasing intensity of the Na metal signal with cycling is ascribed to the formation of SMSs according to the skin-depth effect (see Supplementary Discussion)²⁵.

Figure 4b,c presents the evolution of the ^{23}Na NMR shift of Na metal cycled in F0 and F2 electrolytes, respectively. Figure 4d shows the corresponding normalized integral area of the Na metal signal as a function of cycle time. For F2 electrolyte, the integral of

the Na metal with ^{23}Na NMR signal centred at 1,125 ppm remains constant during cycling, indicating smooth deposition of Na metal, which is consistent with the MRI results. For the F0 electrolyte, on the other hand, asymmetric broadening emerges downfield upon cycling, which can be assigned to SMSs instead of bulk Na metal (Supplementary Fig. 6). Interestingly, this asymmetric broadening in line shape seems to be less visible in the MRI spectra, which is due to the different signal sources and battery configurations of MRI

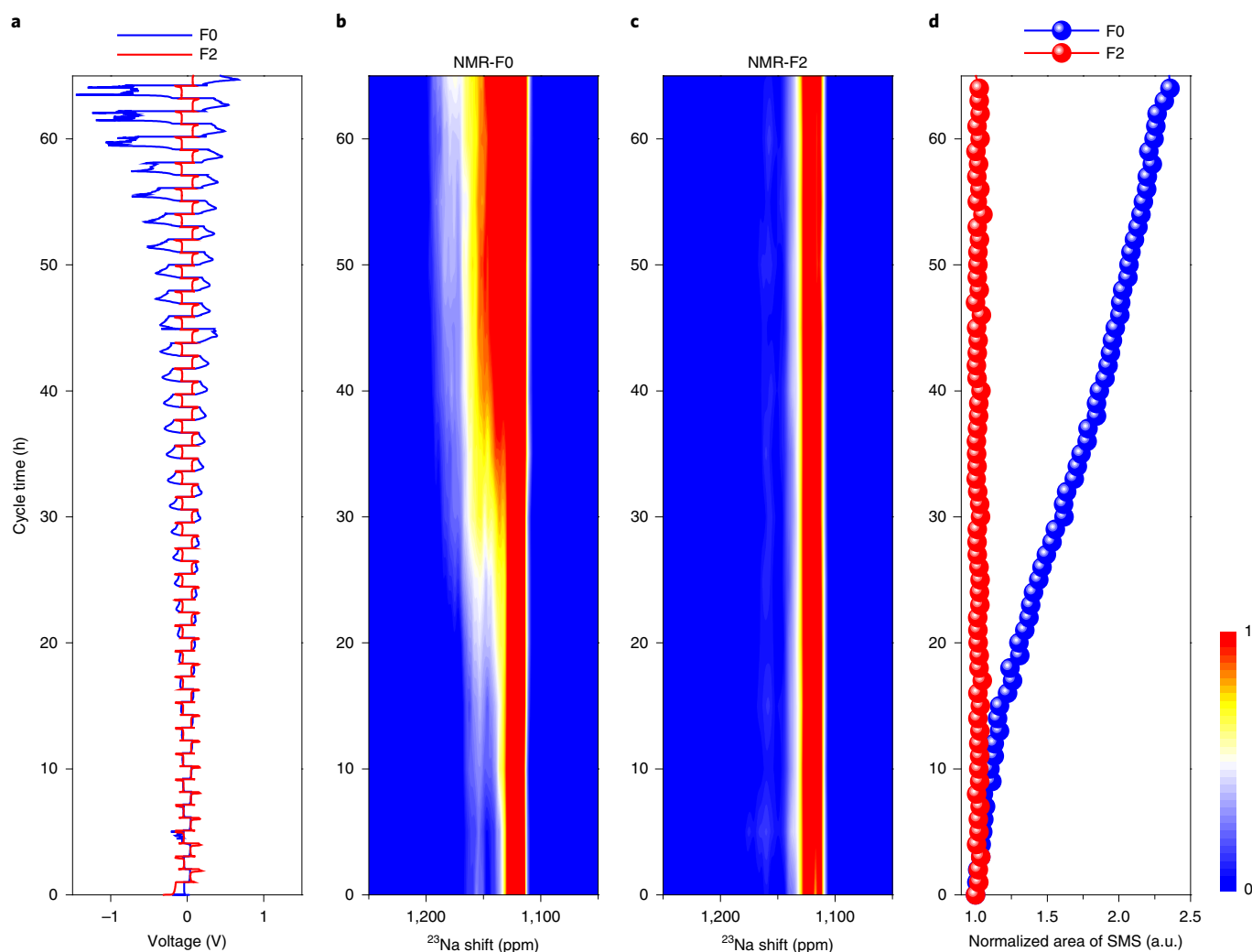


Fig. 4 | The growth of SMSs observed by operando NMR. **a**, Galvanostatic cycling voltage profiles of Na || Na symmetric operando cells cycled with F0 (blue) and F2 (red) electrolytes. **b,c**, Operando NMR spectra of Na || Na cells with F0 (**b**) and F2 (**c**) electrolytes. **d**, Normalized integral area of Na metal signal (from 1,100 ppm to 1,200 ppm) from operando NMR spectra versus the cycle time. The representative ^{23}Na spectra are presented in Supplementary Fig. 6.

and operando NMR experiments. Further discussion is included in Supplementary Fig. 7. Figure 4d shows that the overall integral area of Na metal signals over 1,100–1,200 ppm increases markedly with cycle time for the F0 electrolyte, demonstrating the formation and continuous growth of SMSs. Note that the amount of SMSs and the corresponding cell overpotential have a similar trend with cycling. As the cycle time increases, both the overpotential and the amount of SMSs increase for the F0 electrolyte, while no change is observable for F2, as shown in Fig. 4a,d. Accordingly, we believe that the overpotential and the formation of SMSs are highly correlated.

To validate this hypothesis, the rate of increase of the overpotential (R_V) and the rate of growth of the SMSs (R_S) are calculated using equations (1) and (2):

$$R_V = \frac{dV}{dt} \quad (1)$$

$$R_S = \frac{dS}{dt} \quad (2)$$

where V is the overpotential and S is the integral area of the Na metal peak in the ^{23}Na NMR. R_V and R_S are plotted against cycle time, as

shown in Fig. 5b,d. While R_V and R_S are ~ 0 for the cell cycled in F2 electrolyte, the cell cycled with F0 electrolyte shows richer features, with R_V increasing exponentially, whereas R_S oscillates upon cycling. This behaviour reflects the oscillatory trend of the growth rate of the SMSs. The results further suggest that the growth of SMSs can be divided into three stages, in accordance with the in-situ MRI results shown in Fig. 3b. The correlation between the overpotential and the SMS content can be obtained by combining Fig. 5a,c, as shown in Fig. 5e. The curve shows an exponential growth trend, which includes three stages in accord with the evolution of R_V and R_S values.

In stage I, data points fall into a linear plot when the deposition overpotential is below 0.15 V. In stage II, the linear plot becomes curved upwards, which indicates an increase in the slope of the curve. According to equations (1) and (2), the slope of the curve (k) can be calculated with the following equation:

$$k = \frac{dV}{dS} = \frac{R_V}{R_S} \quad (3)$$

Therefore, an increase in slope indicates a rising R_V/R_S value, deriving from an increase in R_V and a reduction in R_S , as shown

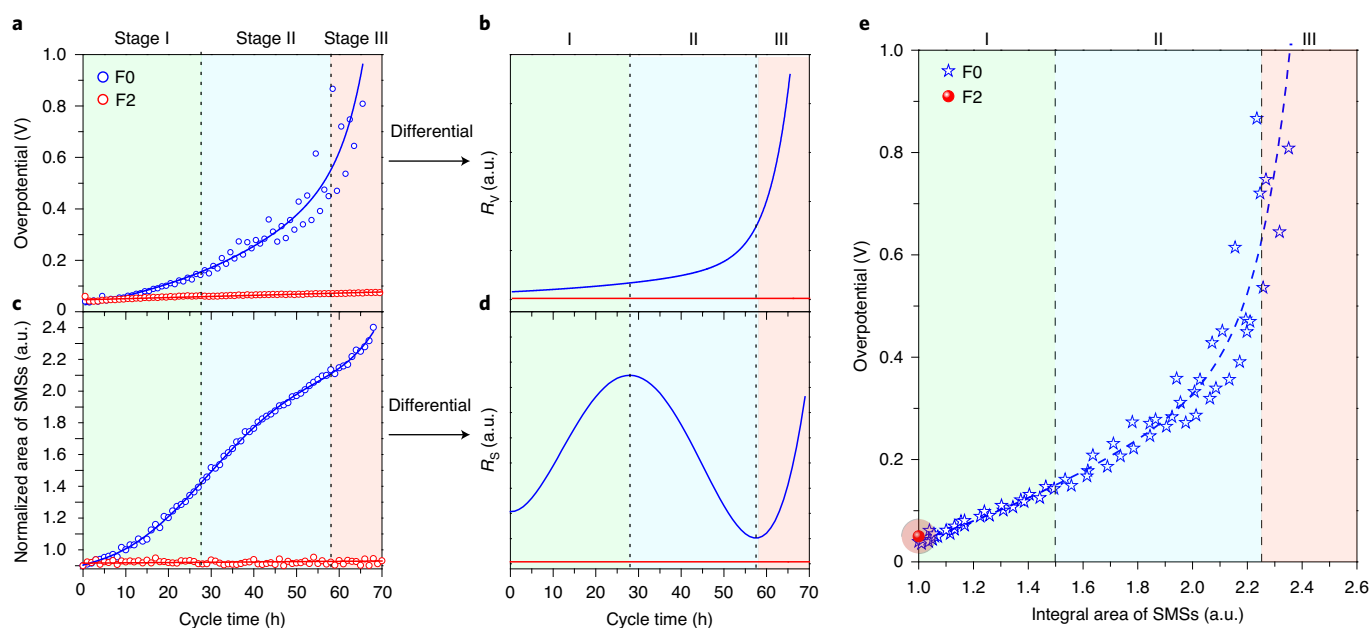


Fig. 5 | The correlation between the SMSs and overpotential. **a, c**, Overpotential (**a**) and content (**c**) of SMSs obtained in operando NMR as a function of cycle time in F0 and F2 electrolytes. **b**, The rate of increase of the overpotential. **d**, The rate of growth of SMSs. **e**, Plot of overpotential versus the content of SMSs. Data points in **a, c** and **e** are fitted by a single line to better show the trend of the increase.

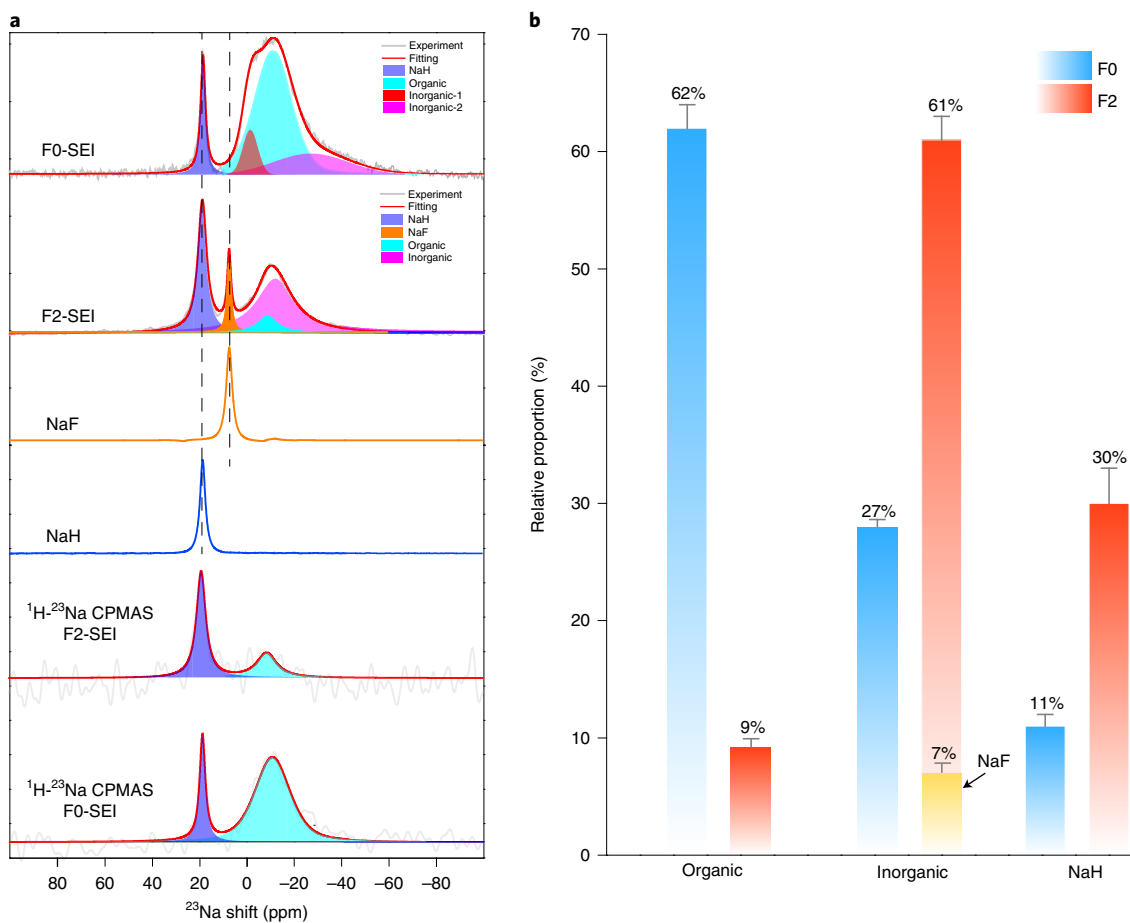


Fig. 6 | Ex-situ NMR characterization of SEI species. **a**, Single-pulse ^{23}Na NMR and $^1\text{H} \rightarrow ^{23}\text{Na}$ CPMAS NMR spectra of SEI species harvested from Cu foil after 50 cycles, and the reference spectra of NaF and NaH. **b**, The relative proportion of organic and inorganic components in the SEI species. Error bars indicate errors when fitting NMR signals of different SEI components.

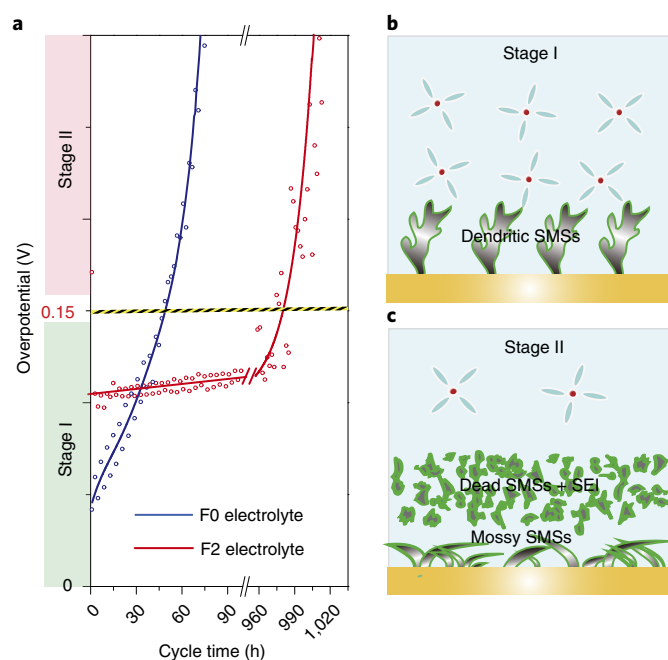


Fig. 7 | The correlation between overpotential and SMSs with two contrasting SEI features derived from F0 and F2 electrolytes, and the corresponding morphological evolution schematics. a, Overpotential versus cycle time for F2 and F0 electrolytes in the Na||Na cells. Data extracted from Fig. 1c. There is a critical transition voltage of around 0.15 V for both two-model electrolytes. **b**, For F0 electrolyte, the SMSs tend to be dendritic below the transition voltage (stage I). **c**, When exceeding the transition voltage (stage II), serious electrochemical decomposition of electrolyte is triggered, which results in a change in the surface morphology of the Na metal, which accelerates the depletion of electrolytes. Then, exhaustion of the electrolyte leads to fast growth of SMSs and quickly shuts down the battery (stage III, not shown in the schematic). The F2 model (with FEC additive) forms an electronically insulated SEI with minimal electrolyte decomposition. The overpotential remains below the transition voltage, thus extending the period of stage I and achieving almost 1,000 hours of cycling time.

in Fig. 5b,d. The increased value of k is likely to arise from the accumulation of highly resistive SEI components, as a larger overpotential is needed for SMSs formation. The results also infer that violent electrochemical decomposition of the electrolyte takes place in stage II, which consumes a large amount of the Faraday current. Thus, at a given current density, these parasitic reactions slow down the growth of SMSs. In stage III, as the electrolyte is depleted, both R_s and R_v increase and the k value increases more dramatically.

The impact of the SEI

The results above have emphasized the importance of avoiding continuous electrolyte decomposition, which is strongly related to the properties of the SEI layers, especially the ionic and electronic conductivities²⁶. We employed solid-state NMR and XPS to qualitatively and quantitatively characterize the SEI layers for Na metal cycled in both F0 and F2 electrolytes. Supplementary Fig. 10 shows the C 1s and F 1s XPS spectra of Na metal after 50 cycles in the Na||Na cells with F0 and F2 electrolytes. The results indicate that a larger amount of organic components are produced in F0, as evidenced by strong signals in the C 1s spectra. On the contrary, the inorganic component NaF is only observed for the F2 electrolyte, in the F 1s spectrum.

To quantify the SEI components, ²³Na magic-angle-spinning (MAS) NMR spectra were measured on the surface species collected from the Cu foil after 50 cycles (Fig. 6a). The spectrum of the F0 sample shows a sharp peak at 18.8 ppm and a broad peak at around -11.0 ppm, whereas the spectrum of the F2 sample shows an extra peak at 7.2 ppm. The peaks at 7.2 ppm and 18.8 ppm are assigned to NaF and NaH, respectively, on the basis of their distinctive chemical shifts. The assignment is further confirmed by measuring the ²³Na NMR spectra of the model compounds, as shown in Fig. 6a. ¹H→²³Na cross-polarization magic-angle-spinning (CPMAS) experiments were carried out to distinguish the organic components from the inorganic components, as shown in Fig. 6a. In the CPMAS experiment, magnetization from ¹H is transferred to ²³Na via dipole-dipole interaction, thus, only the organic components containing sodium and NaH can be observed. Therefore, we can deconvolute the single-pulse ²³Na MAS spectra of the SEI into organic and inorganic components on the basis of its features in the ¹H→²³Na CPMAS spectra (Fig. 6a), and quantify each SEI component (Fig. 6b). Comparing F2 with F0 electrolyte, the proportion of organic components declines from 62 at.% to 39 at.%, while the proportion of inorganic components rises from 27 at.% to 61 at.%. Note that within the increased amount of inorganic SEI species in the FEC sample, only 7 at.% comes from NaF, the remaining inorganic SEI can be Na₂CO₃ (ranging from 10 ppm to -40 ppm, Supplementary Fig. 8) and NaO₂ (-23 ppm)²⁷.

The reduction in organic components and increase in inorganic components is highly relevant to the excellent long-term cycle performance and stable impedance for Na metal batteries with F2 electrolyte. The ionic and electronic conductivities of the components in the SEI layers are also investigated by ²³Na spin-lattice relaxation time (T_1) NMR measurements and theoretical calculations, respectively (Supplementary Table 1). The T_1 value of the broad ²³Na NMR peak at -11.0 ppm, which corresponds to Na in a combination of organic and inorganic species, is ~10 ms, the lowest value amongst the peaks. This implies the highest Na mobility amongst these species²⁸. The peak includes the resonances attributed to both organic and inorganic components, as shown in Fig. 6a, which are difficult to deconvolute and are therefore analysed together. The T_1 value of the NaF signal at 7.2 ppm is ~5 s, indicating sluggish Na mobility, which is responsible for the large interfacial impedance in the cell with the F2 electrolyte after the first cycle (Fig. 1d) and a greater nucleation overpotential for Na deposition (Fig. 1b). Moreover, NaH shows a T_1 value of ~7 s, which indicates an even slower ionic mobility than that of NaF. The T_1 results verify that the existence of NaF and NaH hinders Na⁺ ion transport at the interface. In addition, the band gaps of NaH and NaF, which are determined by our first-principle calculations, are shown in Supplementary Fig. 12. The NaF and NaH present large band gaps of 6.08 eV and 4.04 eV, respectively, which hints at their poor electronic conductivity. The NMR spectra and calculation results suggest that NaF and NaH can passivate the Na metal and prevent further decomposition of the electrolyte. In summary, a certain amount of these inorganic components in the SEI layers would slow down the overpotential increase, thus keeping the system below the transition voltage for enhanced electrochemical performance.

We also evaluate a feasible formation mechanism for NaH by calculating the formation energy, as shown in Supplementary Table 2. The sodium metal may react with hydrogen gas, and/or some sodium-based hydrated compounds, to form NaH, which is consistent with previous calculation results²⁹. Although the role of NaH in the SEI layer is not fully understood, its existence as an electronic insulator seems to be a positive factor for battery performance. Full clarification of the components of the SEI will undoubtedly enhance our understanding of interfacial chemistry and the corresponding performance, such as identification of LiF³⁰ and cross-linked PEO type polymer³¹, in lithium-ion batteries.

Conclusions

We have shown a combination of approaches, including in-situ MRI and operando NMR techniques, to illustrate a space-resolved and quantitative analysis of the growing process for SMSs. An innovative analytical approach is exploited to process the in-situ NMR data, which yields a mathematical understanding of the correlation between the rate of increase of the deposition overpotential and the content of the SMSs. We found that the deposition overpotential is a good indicator of the severity of electrolyte decomposition, as summarized in Fig. 7, which clearly demonstrates a critical transition voltage of around 0.15 V for both two-model electrolytes. Therefore, controlling the overpotential below the transition voltage is necessary for achieving long-term stable cycling. Alternatively, elevating the transition voltage by adjusting the solvent and sodium salt can also be an effective pathway to pursue long-term cycling beyond controlling the overpotential, such as employing a high concentration of electrolyte to reduce the reactivity of the solvent.

Notably, we observe the formation of NaH. The low electronic conductivity of NaH blocks continuous reaction between the electrolyte and the sodium metal.

Our work validates the capabilities of magnetic resonance techniques for providing in-situ quantitative spatial and chemical information for the battery system. It is applicable to future study of deposition and stripping behaviours of alkali metal anodes and identification of surface species in diverse electrolyte systems, including all-solid-state batteries.

Note added in proof: During the peer review stage of the manuscript, we became aware of a study showing sodium microstructures by ^{23}Na MRI technique³².

Online content

Any methods, additional references, Nature Research reporting summaries, source data, extended data, supplementary information, acknowledgements, peer review information; details of author contributions and competing interests; and statements of data and code availability are available at <https://doi.org/10.1038/s41565-020-0749-7>.

Received: 14 February 2020; Accepted: 30 June 2020;

Published online: 27 July 2020

References

- Lee, B., Paek, E., Mitlin, D. & Lee, S. W. Sodium metal anodes: emerging solutions to dendrite growth. *Chem. Rev.* **119**, 5416–5460 (2019).
- Zhao, Y. et al. In situ formation of highly controllable and stable Na_3PS_4 as a protective layer for Na metal anode. *J. Mater. Chem. A* **7**, 4119–4125 (2019).
- Zheng, J. et al. Extremely stable sodium metal batteries enabled by localized high-concentration electrolytes. *ACS Energy Lett.* **3**, 315–321 (2018).
- Luo, W. et al. Encapsulation of metallic Na in an electrically conductive host with porous channels as a highly stable Na metal anode. *Nano Lett.* **17**, 3792–3797 (2017).
- Liu, S. et al. Porous Al current collector for dendrite-free Na metal anodes. *Nano Lett.* **17**, 5862–5868 (2017).
- Zhou, W., Li, Y., Xin, S. & Goodenough, J. B. Rechargeable sodium all-solid-state battery. *ACS Cent. Sci.* **3**, 52–57 (2017).
- Rodriguez, R. et al. In situ optical imaging of sodium electrodeposition: effects of fluoroethylene carbonate. *ACS Energy Lett.* **2**, 2051–2057 (2017).
- Li, X., Zhao, L., Li, P., Zhang, Q. & Wang, M.-S. In-situ electron microscopy observation of electrochemical sodium plating and stripping dynamics on carbon nanofiber current collectors. *Nano Energy* **42**, 122–128 (2017).

- Jin, Y. et al. Identifying the structural basis for the increased stability of the solid electrolyte interphase formed on silicon with the additive fluoroethylene carbonate. *J. Am. Chem. Soc.* **139**, 14992–15004 (2017).
- Gao, L. et al. Revealing the chemistry of an anode-passivating electrolyte salt for high rate and stable sodium metal batteries. *J. Mater. Chem. A* **6**, 12012–12017 (2018).
- Yu, C. et al. Accessing the bottleneck in all-solid state batteries, lithium-ion transport over the solid–electrolyte–electrode interface. *Nat. Commun.* **8**, 1086 (2017).
- Bhattacharyya, R. et al. In situ NMR observation of the formation of metallic lithium microstructures in lithium batteries. *Nat. Mater.* **9**, 504–510 (2010).
- Chandrashekar, S. et al. ^7Li MRI of Li batteries reveals location of microstructural lithium. *Nat. Mater.* **11**, 311–315 (2012).
- Chang, H. J. et al. Correlating microstructural lithium metal growth with electrolyte salt depletion in lithium batteries using ^7Li MRI. *J. Am. Chem. Soc.* **137**, 15209–15216 (2015).
- Kim, H. et al. Ethylene bis-carbonates as telltales of SEI and electrolyte health, role of carbonate type and new additives. *Electrochim. Acta* **136**, 157–165 (2014).
- Komaba, S. et al. Electrochemical Na insertion and solid electrolyte interphase for hard-carbon electrodes and application to Na-ion batteries. *Adv. Funct. Mater.* **21**, 3859–3867 (2011).
- Iermakova, D. I., Dugas, R., Palacin, M. R. & Ponrouch, A. On the comparative stability of Li and Na metal anode interfaces in conventional alkyl carbonate electrolytes. *J. Electrochem. Soc.* **162**, A7060–A7066 (2015).
- Seh, Z. W., Sun, J., Sun, Y. & Cui, Y. A highly reversible room-temperature sodium metal anode. *ACS Cent. Sci.* **1**, 449–455 (2015).
- Cao, R. et al. Enabling room temperature sodium metal batteries. *Nano Energy* **30**, 825–830 (2016).
- Choudhury, S. et al. Designing solid-liquid interphases for sodium batteries. *Nat. Commun.* **8**, 898 (2017).
- Wood, K. N. et al. Dendrites and pits: untangling the complex behavior of lithium metal anodes through operando video microscopy. *ACS Cent. Sci.* **2**, 790–801 (2016).
- Yui, Y., Hayashi, M. & Nakamura, J. In situ microscopic observation of sodium deposition/dissolution on sodium electrode. *Sci. Rep.* **6**, 22406 (2016).
- Zhao, C. et al. Advanced Na metal anodes. *J. Energy Chem.* **27**, 1584–1596 (2018).
- Wu, B., Lochala, J., Taverne, T. & Xiao, J. The interplay between solid electrolyte interface (SEI) and dendritic lithium growth. *Nano Energy* **40**, 34–41 (2017).
- Bayley, P. M., Trease, N. M. & Grey, C. P. Insights into electrochemical sodium metal deposition as probed with in situ ^{23}Na NMR. *J. Am. Chem. Soc.* **138**, 1955–1961 (2016).
- Cheng, X.-B., Yan, C., Zhang, X.-Q., Liu, H. & Zhang, Q. Electronic and ionic channels in working interfaces of lithium metal anodes. *ACS Energy Lett.* **3**, 1564–1570 (2018).
- Reeve, Z. E. et al. Detection of electrochemical reaction products from the sodium-oxygen cell with solid-state ^{23}Na NMR spectroscopy. *J. Am. Chem. Soc.* **139**, 595–598 (2017).
- Wang, D. et al. The synergistic effects of Al and Te on the structure and Li^+ -mobility of garnet-type solid electrolytes. *J. Mater. Chem. A* **2**, 20271–20279 (2014).
- Tian, Y. et al. Reactivity-guided interface design in Na metal solid-state batteries. *Joule* **3**, 1037–1050 (2019).
- Zhang, X.-Q., Cheng, X.-B., Chen, X., Yan, C. & Zhang, Q. Fluoroethylene carbonate additives to render uniform Li deposits in lithium metal batteries. *Adv. Funct. Mater.* **27**, 1605989 (2017).
- Jin, Y. et al. Understanding fluoroethylene carbonate and vinylene carbonate based electrolytes for Si anodes in lithium ion batteries with NMR spectroscopy. *J. Am. Chem. Soc.* **140**, 9854–9867 (2018).
- Bray, J. M. et al. Operando visualisation of battery chemistry in a sodium-ion battery by ^{23}Na magnetic resonance imaging. *Nat. Commun.* **11**, 2083 (2020).

Publisher's note Springer Nature remains neutral with regard to jurisdictional claims in published maps and institutional affiliations.

© The Author(s), under exclusive licence to Springer Nature Limited 2020

Methods

Electrochemical test. The Na||Na and Na||Cu coin cells, of CR2025 size, were assembled in an argon (Ar)-filled glove box. A solution of 1.0 M NaClO₄ in PC, with and without 2 vol% FEC, was applied as the electrolyte. Galvanostatic electrochemical measurements were conducted on a LAND CT-2001A battery test system at 30 °C. The EIS measurements were performed in the frequency range 10⁶–10¹ Hz with a potential perturbation of 10 mV.

Characterization. The morphologies of the Na metal anodes and corresponding Na deposits were characterized by SEM (on a HITACHI S-4800) operated at 10.0 kV. All samples were protected with Ar in the transfer process. XPS measurements were performed with a PHI-5000 Versa Probe II spectrometer (ULVAC-PHI, Inc., Japan) with monochromatic Al K α radiation (1,486.6 eV), operating at 23.2 W and 16 kV with a beam spot size of 100 μ m and in a vacuum of <10⁻⁸ Torr. The cells were disassembled and stored in a glove box under Ar. All samples were protected with Ar in the process of transfer. First-principles calculations were implemented using the Vienna Ab-initio Simulation Package, and projector augmented wave method with the Perdew–Burke–Ernzerhof functional. K-points sampling was 5 \times 5 \times 5 \AA^3 and the plane-wave basis cut-off was 500 eV. Cell parameters were optimized first with a 0.01 eV \AA^{-1} force convergence criterion. The total energy convergence criterion was 10⁻⁴ eV for all calculations.

Magnetic resonance. *Magnetic resonance imaging.* The 1D ²³Na MRI spectra were acquired using a Diff50 probe head with a home-made MRI battery. The schematic of the MRI battery is shown in Supplementary Fig. 3. A 5 \times 5 \times 0.1 mm³ sodium metal disk and 5 \times 5 \times 1 mm³ Cu disk were used to assemble the Na||Cu MRI batteries, which cycled with 0.5 mA h cm⁻² at 0.5 mA cm⁻². All MRI experiments were carried out on a Bruker Avance III 400 MHz spectrometer operating at 105.6 MHz for ²³Na under a gradient strength of 9.8 T m⁻¹. A total of 14 slices of 1D spectra with successive offset were acquired for every charge state, then reconstructed into two-dimensional spectra. The 1D spectra were obtained with a $\pi/2$ pulse of 22.5 μ s, recycle delay of 0.1 s and 5,120 transients. Detailed information for the pulse program is shown in Supplementary Fig. 11. For the last pulse, high power and small angle were used to obtain uniform excitation in a wide range. The phase cycle was used to eliminate the unwanted signals excited in the last pulse. The total experimental time for MRI was 2 h 54 min.

Operando NMR. Operando NMR experiments were performed on a home-made in-situ probe head and operando cell. The schematic of the operando cell is presented in Supplementary Fig. 3. Sodium metal disks of 5 \times 5 \times 0.1 mm³ were used to assemble the Na||Na symmetric battery. A solution of 1 M NaClO₄ in PC with and without 2% FEC was used as the electrolyte, and glass fibre was as the separator. The operando batteries were cycled with a current density of 0.5 mA cm⁻² and the area capacity of 0.5 mA h cm⁻². Hahn-echo with a $\pi/2$ pulse of 7.2 μ s and recycle delay of 0.1 s was applied to acquire the 1D static spectra, with an interval time of 3,600 s. Every single spectrum required

102 s. The total experimental time for F0 and F2 electrolytes was 70 h and 100 h, respectively.

Ex-situ NMR. Na||Cu cells were disassembled after 50 cycles. Cu foil was washed with anhydrous dimethyl carbonate three times and dried overnight under vacuum in the glove box. The SEI was collected from the Cu foil and transferred into the 2.5-mm rotor and sealed with a Vespel cap. All ex-situ NMR experiments were performed on a Bruker Avance III 400 MHz spectrometer with a 2.5-mm probe head under spinning rates of 25 kHz. The ²³Na single-pulse experiment was performed with a $\pi/4$ pulse length of 2.0 μ s and a repetition times of 10 s to ensure quantitative analysis. The ²³Na spin–lattice relaxation time (T_1) measurements were conducted using saturation recovery experiments. The ¹H–²³Na CPMAS NMR was performed with a contact time of 0.6 ms and SPINAL-¹H decoupling at 70.0 kHz. The ²³Na chemical shifts were externally referenced to 1 M NaCl aqueous solution (0 ppm).

Data availability

The data that support the plots within this paper and other findings of this study are available from the corresponding author upon reasonable request.

Acknowledgements

This research is financially supported by National Key Research and Development Program of China (grant nos. 2018YFB0905400 and 2016YFB0901500) and National Natural Science Foundation of China (grant nos. 21935009, 21761132030 and 21603231). R.F. acknowledges support from the National High Magnetic Field Laboratory, which is supported by NSF Cooperative Agreement DMR-1644779 and the State of Florida. We acknowledge R. Liu and J. Dahn for helpful discussion.

Author contributions

Y.Y., Y.X. and G. Zhong proposed and planned the project. Y.Y. and G. Zhong supervised the project. Y.X., X.L., S.Y. and Z.L. carried out the NMR measurements. Y.X. and G. Zhong prepared the in-situ cells. S.C. and H.H. performed the SEM measurements and K.Z. and J.Z. performed and analysed XPS experiments. M.L. conducted the theoretical calculations. R.F. and J.W. assisted in data analysis. Y.X. and G. Zhong wrote the manuscript. Y.J. and Y.L. contributed to the discussion and revision of the manuscript.

Competing interests

The authors declare no competing interests.

Additional information

Supplementary information is available for this paper at <https://doi.org/10.1038/s41565-020-0749-7>.

Correspondence and requests for materials should be addressed to G.Z. or Y.Y.

Reprints and permissions information is available at www.nature.com/reprints.